Multi-Beam Design for Near-Field Extremely Large-Scale RIS-Aided Wireless Communications

Decai Shen, Linglong Dai, *Fellow, IEEE*, Xin Su, and Shiqiang Suo

***Abstract*—As the energy-saving array composed of passive elements, reconfigurable intelligent surface (RIS) will evolve to the extremely large-scale RIS (XL-RIS) to overcome serious path loss. This change leads to the near-field propagation becoming dominant. There are some works to explore the near-field beam design via beam training. Unfortunately, due to the constant modulus constraint for XL-RIS, most of works in the near-field scenario focus on single-beam design. For massive connectivity requirement scenario, these works will face a serious loss of beam gains, resulting in a decrease in transmission rate. To solve this problem, we propose a block coordinate descent-based scheme with majorization-minimization (MM) algorithm for multi-beam design. The proposed scheme handles constant modulus constraint from two aspects. Firstly, under this constraint, the multi-beam design is an intractable non-convex quadratic programming problem. We utilize MM algorithm to solve this problem as several iterative sub-problems which are easily to be solved. Secondly, the solution space for multi-beam optimization is confined to a limited space due to this constraint, so we introduce the phases for beam gains as an extra optimizable variable to enrich the degree of freedom for optimization. Simulation results show that the proposed scheme could achieve a superior rate 50% higher than the existing schemes.**

***Index Terms*—Reconfigurable intelligent surface (RIS), constant modulus constraint, multi-beam design.**

I. Introduction

RECONFIGURABLE intelligent surface (RIS) has been regarded as one of the most promising technologies for future wireless communications [2], [3]. RIS is endowed with the capability to manipulate the signal propagation environment by creating a controllable reflecting link [4], [5]. Benefiting from this capability, RIS is expected to bring potential advantages of overcoming blockages [6], [7], ensuring the secure transmission [8], enhancing the coverage [9], [10], and improving the spectrum efficiency [11], [12].

However, the desired performance of RIS will be heavily restricted due to the *multiplicative fading effect* in practical wireless systems [13], [14]. Since the serious path loss of the transmitter-RIS-receiver reflecting link is the *multiplication* (rather than the *sum*) of the path losses of the transmitter-RIS link and the RIS-receiver link. Considering that the array gain for RIS is proportion to the square of the number of RIS elements [14], [15], this serious multiplicative path loss can be effectively compensated by enlarging the array aperture with a massive number of low-cost RIS elements [6], [16]. As a consequence, the evolution of RIS will perhaps develop towards extremely large-scale RIS (XL-RIS) for the future wireless networks [17].

To explore the potential performance for XL-RIS, it is important to design RIS beamforming according to the accurate channel state information (CSI). With the increase of the number of RIS elements, it is pretty difficult to estimate the perfect CSI due to the high computation complexity. As another kind of scheme, many works design the beamforming without the requirement for accurate CSI. Specifically, the beam pointed to the desired spatial angle will be selected by beam training from a pre-designed codebook. These works are efficient for the existing RIS system. However, with the increase of the array aperture of RIS, the electromagnetic radiation feature will evolve from the existing far-field planar wavefront to a near-field spherical wavefront. To ensure the beamforming performance, the beam should be adjusted not only in the angle domain but also in the distance domain, based on which the existing works are no longer efficient. Hence, it is crucial to explore the near-field beam design for XL-RIS aided wireless communications.

A. Prior Works

Relying on the accurate CSI acquired by channel estimation, the RIS beamforming can be formulated as a series of optimization problems with different objective functions. Numerous beamforming design schemes [18], [19], [20], [21] have been studied in several scenarios for different performance indicators (e.g., the transmission capacity, the energy efficiency, the spectrum efficiency). However, due to the high computation complexity, it is pretty difficult to estimate the perfect CSI in practical XL-RIS aided wireless communications.

As another kind of effective scheme without the requirement for channel estimation, the beamforming design is determined

Manuscript received 10 November 2022; revised 10 February 2023; accepted 10 March 2023. Date of publication 21 March 2023; date of current version 21 August 2023. This work was supported in part by the National Key Research and Development Program of China under Grant 2020YB1807201; in part by the National Natural Science Foundation of China under Grant 62031019; and in part by the European Commission through the H2020-MSCA-ITN META WIRELESS Research Project under Grant 956256. This article was presented in part at the IEEE Global Communications Conference (GLOBECOM), Rio de Janeiro, Brazil, from 4–8 December 2022[DOI: 10.1109/GLOBECOM48099.2022.10000922]. The editor coordinating the review of this article was C. Wu. *(Corresponding author: Linglong Dai.)*

Decai Shen and Linglong Dai are with the Department of Electronic Engineering and the Beijing National Research Center for Information Science and Technology, Tsinghua University, Beijing 100084, China (e-mail: sdc18@mails.tsinghua.edu.cn; daill@tsinghua.edu.cn).

Xin Su and Shiqiang Suo are with the Innovation Center, CICT Mobile Communication Technology Company Ltd., Beijing 100084, China (e-mail: suxin@cictmobile.com; suoshiqiang@cictmobile.com).

Digital Object Identifier 10.1109/TGCN.2023.3259579

by beam training with utilizing a pre-designed codebook [22], [23], [24], [25]. In other words, the RIS beamforming vector is selected from one of the limited amount codewords of this codebook, instead of being calculated according to the CSI. In [22], the alternative minimization method with a closed-form expression (AMCF) is proposed to design a hierarchical far-field codebook. In [23], a two-step codeword design approach is presented based on which a fast search based alternative minimization (FS-AltMin) algorithm is proposed for beam training. In [24], a non-coherent demodulation scheme (NCDS) is proposed for RIS beam training, based on which the received differential data can be used for the determination of the best spatial angle beam for the RIS. As a result, the training overhead can be further reduced. Besides, to improve the directivity of the RIS beams, some cameras are employed at the RIS to correct beam direction with the help of machine learning-based computer vision after the classical beam training [25].

The above works are effective for the existing RIS-aided wireless communications. However, in multi-user XL-RIS aided wireless communications, these methods will face serious performance loss. The evolution from RIS to XL-RIS will not simply bring the enlargement of the aperture, but also lead to a critical change in the electromagnetic radiation feature. Specifically, the region of the radiation field can be divided into two parts (i.e., the far-field and the near-field region). These two regions are divided via the boundary called the Rayleigh distance [17], which is proportional to the square of the array aperture. With the increase for array aperture, the near-field region will expand rapidly and the near-field transmission with the spherical wavefront model should be primarily considered [17], based on which the beam will focus on a small area instead of pointing to a spatial direction like the far-field transmission.

Hence, in the near-field scenario, the XL-RIS beam design should be restudied [26], [27], [28], [29]. In [26], a near-field codebook for the RIS channel is designed and a hierarchical training scheme is proposed for single-user RIS-aided systems. Moreover, a variable-width codebook is devised in [27], which is suitable for both the near- and far-field. In [28], to improve the scanning efficiency in a large-size distance interval, a novel spatial-chirp beam-aided codebook and corresponding hierarchical update policy are proposed. Besides, to reduce the overhead of the complicated distance search, a customized polar-domain codebook is employed to find the best effective distance in a shortlisted candidate angle [29].

Most of the existing works for the near-field beam design are focused on the single-user scenario, i.e., the single-beam design. The multi-beam design for the near-field XL-RIS system is still an open problem to be further researched. For the multi-user transmission, a straightforward scheme is to extend these single-beam design schemes by superposing several single beams at RIS, i.e., we can simultaneously superpose the single-beam codewords for all users as the superposed RIS beamforming vector for the multi-user case. Actually, this straightforward design has been studied for current massive MIMO systems [30], [31] with satisfactory performance.

Unfortunately, in multi-user XL-RIS aided wireless communications, this extension will face serious performance loss. The reason can be expressed as follows. For the superposed beamforming vector, both the amplitudes and the phases have been changed compared with the single-beam codewords for individual users. In other words, to employ this beamforming vector at RIS, it requires the element of RIS to have the ability to simultaneously adjust amplitude and phase. Unfortunately, for most all of the practical RIS, we can only adjust the phase coefficient rather than the amplitude coefficient due to the hardware limitations [32], which is called the *constant modulus constraint*. Limited by this constraint, if we directly migrate the existing single-beam design to a multi-user case according to the above method by superposing codewords, the effective directions of the superposed beam will seriously deviate from the desired areas of users. As a result, the minimal rate of all users will be rapidly decreased which results in a large gap between expectant and practical performance for XL-RIS aided wireless communications.

B. Our Contributions

In order to improve the minimal rate, we study the near-field multi-beam design for XL-RIS to serve the multiple users.[1] The specific contributions of this paper can be summarized as follows.

- Firstly, different from the existing near-field single-beam design works for the single-user scenario, we devise a multi-beam design method for near-field XL-RIS beamforming in this paper, which is still an open problem lacking exploration. Without other indirect objective functions, the core aim of the method is to generate the near-field multiple beams from the XL-RIS pointing to the desired areas of users with the desired beam gains under the constant modulus constraint. This method is composed of a beam training procedure and a multi-beam design procedure. The first procedure is executed by all users independently to acquire the desired single-beam direction of each user. Then, the multi-beam design procedure is formulated as a non-convex quadratic programming to acquire the beamforming vector, for which the programming objective, is acquired by the first procedure.
- Secondly, to solve the non-convex quadratic programming, we propose a block coordinate descent (BCD) based scheme with the majorization-minimization (MM) algorithm to achieve the multi-beam design procedure. The proposed scheme handles the influence of constant modulus constraint from two aspects. At first, with this constraint, the multi-beam design problem is an intractable non-convex optimization. Hence, we tackle the intractable problem by decomposing it into a series of tractable sub-problems to be iteratively solved with the help of the MM algorithm. Then, note that the solution space for the multi-beam design is incomplete due to constant modulus constraint, we introduce the phase information of the original optimization objective as the

[1] Simulation codes are provided to reproduce the results in this paper: http://oa.ee.tsinghua.edu.cn/dailinglong/publications/publications.html.

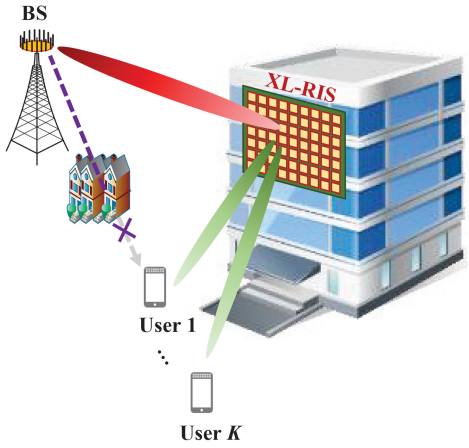

Fig. 1. The system model for XL-RIS aided wireless communications.

extra optimizable variables. Thus, the degree of freedom of optimization can be enriched. Finally, we execute the beams design procedure by alternately optimizing the above two aspects with the BCD strategy. Besides, the closed-form solution for every iteration is also provided.

- Simulation results verify that the proposed near-field multi-beam design can achieve a minimal rate to all users 50% higher than the existing near-field schemes. Particularly, we also carry out the simulations for far-field users, which illustrates that the proposed scheme also has a performance gain compared with the existing far-field single-beam design schemes.

C. Organization and Notation

Organization: For the rest of this paper, the signal model and channel model are given in Section II. In Section III, the proposed multi-beam design method for the XL-RIS is proposed. The simulation results are discussed in Section IV. Finally, we provide the conclusion of this paper in Section V.

Notation: $\nabla_{\boldsymbol{x}} f(\boldsymbol{x})$ denotes the gradient of function $f(\boldsymbol{x})$ with respect to the variable $\boldsymbol{x}$; $\mathbf{a} \otimes \mathbf{b}$ represents the Kronecker product of $\mathbf{a}$ and $\mathbf{b}$; $\mathbf{a} \odot \mathbf{b}$ represents the Hadamard product of $\mathbf{a}$ and $\mathbf{b}$; $\mathbf{A}_{(k,l)}$ denotes the element of the matrix $\mathbf{A}$ in k-th row and l-th column; $\mathbf{a}_{(k)}$ denotes the kth element of the vector $\mathbf{a}$; $\mathbf{I}_N$ denotes the $N \times N$-dimensional unit matrix; $[R_{\min}, R_{\max}]$ represents the closed interval from $R_{\min}$ to $R_{\max}$.

II. System Model

In this section, the signal model of XL-RIS aided wireless communications is given at first, based on which the channel models for the far-field scenario and the near-field scenario are presented, respectively.

A. Signal Model

We consider an XL-RIS aided wireless communications, as illustrated in Fig. 1, where a base station (BS) with M antennas assisted by an XL-RIS with N elements simultaneously serves K single-antenna users. Let $\mathcal{N} = \{1, 2, \ldots, N\}$ and $\mathcal{K} = \{1, 2, \ldots, K\}$ denote the index sets of XL-RIS elements and users, respectively. The uniform linear array (ULA) of antennas is employed at the BS, and the uniform planar array (UPA) of elements is employed at the XL-RIS [33]. We consider that the XL-RIS is deployed with N_1 horizontal rows and N_2 vertical columns ($N = N_1 \times N_2$). We adopt the assumption that the direct BS-user transmission link is blocked by the obstacles [26], [34]. For the kth user with $k \in \mathcal{K}$, the received signal y_k can be expressed as

$$y_k = \mathbf{h}_{r,k}^T \boldsymbol{\Theta} \mathbf{G} \mathbf{x} + n_k, \tag{1}$$

where $\mathbf{x} \in \mathbb{C}^{M \times 1}$ is the precoded transmitted signal at the BS; $\mathbf{h}_{r,k}^T \in \mathbb{C}^{1 \times N}$, and $\mathbf{G} \in \mathbb{C}^{N \times M}$ denote the RIS-user channel from the XL-RIS to the kth user, and the BS-RIS channel from the BS to the XL-RIS, respectively; $\boldsymbol{\Theta} \in \mathbb{C}^{N \times N}$ represents the beamforming matrix of the XL-RIS; $n_k \sim \mathcal{CN}(0, \sigma_n^2)$ denotes the additive white Gaussian noise (AWGN) received at the kth user.

The XL-RIS composed of extremely large number of passive reflecting elements can adjust the phase of a incident signal by designing $\boldsymbol{\Theta}$ as

$$\boldsymbol{\Theta} \triangleq \operatorname{diag}(\boldsymbol{\theta}) = \operatorname{diag}(\theta_1, \ldots, \theta_n, \ldots, \theta_N), \tag{2}$$

where $\boldsymbol{\theta}$ represents the RIS beamforming vector, $\theta_n = e^{jp_n}$ ($p_n \in [0, 2\pi], n \in \mathcal{N}$) represents the reflecting coefficient of the nth XL-RIS element.

According to (2), the received signal model in (1) can be rewritten as

$$y_k = \boldsymbol{\theta}^T \operatorname{diag}\left(\mathbf{h}_{r,k}^T\right) \mathbf{G} \mathbf{x} + n_k, \tag{3}$$

where the reflecting channel for the kth user is defined as $\mathbf{H} = \operatorname{diag}(\mathbf{h}_{r,k}^T)\mathbf{G}$. Then, we will introduce the channel model in the far-field scenario and the near-field scenario, respectively.

B. Far-Field Channel Model

Before giving the channel model for the XL-RIS aided wireless communications in the near-field scenario, we first introduce the existing far-field channel model, which has been widely considered in the current research. Considering the geometric channel model [35] for high-frequency transmission, the BS-RIS channel $\mathbf{G}^{\mathrm{FF}}$ can be denoted as

$$\mathbf{G}^{\mathrm{FF}} = \sum_{i=1}^{L_1} \alpha_i \mathbf{b}\left(\phi_{\mathrm{in},i}, \varphi_{\mathrm{in},i}\right) \mathbf{a}^H(\gamma_i), \tag{4}$$

where L_1 is the number of dominant paths, α_i is the complex gain of the ith path; $\phi_{\mathrm{in},i}$ and $\varphi_{\mathrm{in},i}$ represent the azimuth and elevation incident spatial angles at the XL-RIS for the ith path; γ_i denotes the spatial angle of departure for the ith path at the BS. $\mathbf{a}(\gamma)$ and $\mathbf{b}(\phi, \varphi)$ are the far-field array steering vectors for the BS and the XL-RIS, respectively. Based on the well-known planar wavefront assumption, these vectors can be denoted as

$$\mathbf{a}(\gamma) = \frac{1}{\sqrt{M}} \left[e^{j2\pi m\gamma}\right]_{m \in \mathcal{I}(M)}^T, \tag{5a}$$

$$\mathbf{b}(\phi, \varphi) = \frac{1}{\sqrt{N}} \left[e^{j2\pi n_1 \phi}\right]_{n_1 \in \mathcal{I}(N_1)}^T \otimes \left[e^{j2\pi n_2 \varphi}\right]_{n_2 \in \mathcal{I}(N_2)}^T, \tag{5b}$$

where we have $\mathcal{I}(n) = \{0, 1, \ldots, n-1\}$ representing as the integer sequence. We have $\gamma = d_B \sin(\psi)/\lambda$, $\phi = d_R \sin(\vartheta)\cos(\nu)/\lambda$, and $\varphi = d_R \sin(\nu)/\lambda$. The element spacing of XL-RIS, and the antenna spacing of BS are denoted as d_R, and d_B, respectively. The wavelength of the transmission carrier is denoted as λ. The physical angle in the BS is ψ, and the physical angles for the XL-RIS in the azimuth and elevation can be expressed as ϑ, and ν, respectively.

Similar to (4), the RIS-user channel in the far-field can be denoted as [36]

$$\mathbf{h}_{r,k}^{\mathrm{FF}} = \sum_{l=1}^{L_2} \beta_{k,l} \mathbf{b}\left(\phi_{\mathrm{re},k,l}, \varphi_{\mathrm{re},k,l}\right), \tag{6}$$

where L_2 and $\beta_{k,l}$ represent the number of dominant paths and the complex gain of the l-th path, $\phi_{\mathrm{re},k,l}$ and $\varphi_{\mathrm{re},k,l}$ represent the azimuth and elevation reflecting spatial angles for the lth path.

Note that the BS and XL-RIS are usually located in the high wall and tower, based on which there are few scatterers in the propagation environment. Hence, we consider that there is only the line-of-sight (LoS) path from the XL-RIS to the BS or users (i.e., $L_1 = L_2 = 1$) [26], where the broadcast transmission or frequency division transmission can be utilized to serve multiple users. Meanwhile, since the deployment positions for the BS and XL-RIS are fixed, the beam direction of the BS can be designed to point towards the XL-RIS [37], based on which we focus on the RIS beamforming design in this paper. Hence, we can denote the effective BS beamforming as $\mathbf{v} = \mathbf{a}^H(\gamma)$, which means that the BS can be effectively regarded as a single-antenna transmitter.

Hence, the effective reflecting channel for the far-field can be rewritten as

$$\bar{\mathbf{h}}_{\mathrm{FF},k} = \bar{\alpha}_k \mathrm{diag}\left(\mathbf{b}^T\left(\phi_{\mathrm{re},k}, \varphi_{\mathrm{re},k}\right)\right)\mathbf{b}(\phi_{\mathrm{in}}, \varphi_{\mathrm{in}}), \tag{7}$$

where $\alpha_k = \bar{\alpha}\beta_k$ is the effective gain. The subscript i and l have been omitted for simplicity since $i = l = 1$.

C. Near-Field Channel Model

As mentioned in Section I, the far-field and near-field regions are divided by the Rayleigh distance R. The Rayleigh distance R for the transmission array can be defined as [17]

$$R = \frac{2D^2}{\lambda}, \tag{8}$$

where D is the array aperture. When the distance between this array and receiver is smaller than R, the receiver locates in the near-field region of this array and the channel has to be modeled as near-field channel. Moreover, for a XL-RIS aided system, when the distance r_{RA} between the XL-RIS and the BS and the distance r_{RD} between the XL-RIS and the user satisfy

$$\frac{r_{\mathrm{RA}} r_{\mathrm{RD}}}{r_{\mathrm{RA}} + r_{\mathrm{RD}}} < R = \frac{2D^2}{\lambda}, \tag{9}$$

the reflecting channel should be modeled as the near-field channel [17]. From (9) we can find that, as long as any one of the BS or user is distributed in the region of near-field for XL-RIS, the communication related to this reflecting link should be formulated by considering the near-field feature [17]. Hence, for the XL-RIS aided wireless communications, the near-field scenario is more universal.

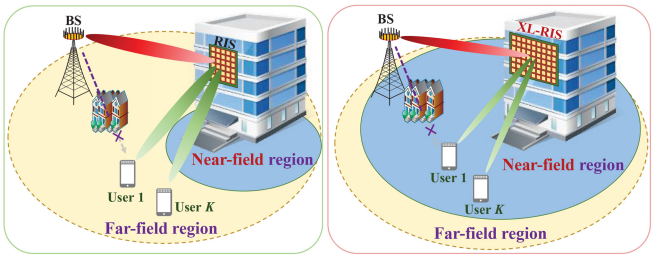

Fig. 2. The near-field XL-RIS aided and the far-field RIS aided wireless communications.

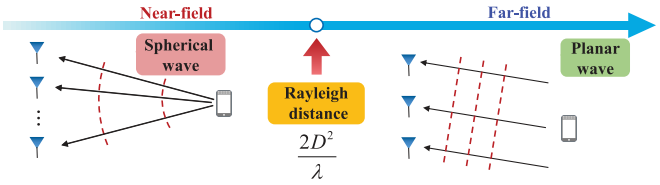

Fig. 3. A comparison figure for the far-field propagation and the near-field propagation [17].

It can be observed from (9) that the Rayleigh distance is proportional to the square of the array aperture. For the array with a fixed element spacing, with the increase of the array aperture from RIS to XL-RIS, the Rayleigh distance will increase quadratically. Hence, the region for near-field will be expanded as illustrated in Fig. 2. As a result, the BS and users are more likely to strew in the near-field region. For example, if the carrier frequency is 10 GHz (i.e., $\lambda = 3 \times 10^{-2}$ m), and the array aperture for RIS is $D_{\mathrm{RIS}} = 0.3$ m, the Rayleigh distance is $R_{\mathrm{RIS}} = 6$ m. For an XL-RIS with array aperture $D_{\mathrm{XL-RIS}} = 1.2$ m, the Rayleigh distance will increase to $R_{\mathrm{XL-RIS}} = 96$ m.

In the far-field scenario, the channel is modeled under the planar wavefront assumption, based on which the far-field steering vector is described as (5) in mathematics. For this scenario, a more intuitive explanation in physics can be illustrated in the right side of Fig. 3, i.e., the equiphase wavefront of the electromagnetic wave can be approximatively treated as coplanar. On the contrary, in the near-field scenario as illustrated in left side of Fig. 3, modeling the electromagnetic wave under the spherical wavefront assumption is more accurate, while following the planar wavefront assumption will bring a serious phase error in the near-field region [17].

In the near-field scenario, the effective reflecting channel $\bar{\mathbf{h}}_{\mathrm{NF},k}$ can be rewritten as [26]

$$\bar{\mathbf{h}}_{\mathrm{NF},k} = \bar{\alpha}_k \mathrm{diag}\left(\mathbf{b}^T\left(\mathbf{r}_{\mathrm{re},k}\right)\right)\mathbf{b}(\mathbf{r}_{\mathrm{in}}), \tag{10}$$

where $\mathbf{r}_{\mathrm{re},k}$ is the space coordinate vector from the XL-RIS to the kth user, and $\mathbf{r}_{\mathrm{in}}$ is the space coordinate vector from the BS to the XL-RIS. $\mathbf{b}^T(\mathbf{r}_{\mathrm{re},k})$ and $\mathbf{b}(\mathbf{r}_{\mathrm{in}})$ in (10) can be

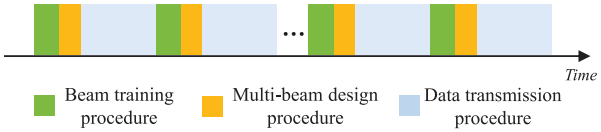

Fig. 4. The process for multi-beam design method and data transmission over time. During each small timescale, the channel remains unchanged.

denoted as

$$\mathbf{b}(\mathbf{r}_{\mathrm{re},k}) = \Big[e^{-j2\pi D_k^{\mathrm{re}}(1,1)}, \ldots, e^{-j2\pi D_k^{\mathrm{re}}(1,N_2)}, \ldots, e^{-j2\pi D_k^{\mathrm{re}}(N_1,1)}, \ldots, e^{-j2\pi D_k^{\mathrm{re}}(N_1,N_2)}\Big]^T, \quad (11a)$$

$$\mathbf{b}(\mathbf{r}_{\mathrm{in}}) = \Big[e^{-j2\pi D^{\mathrm{in}}(1,1)}, \ldots, e^{-j2\pi D^{\mathrm{in}}(1,N_2)}, \ldots, e^{-j2\pi D^{\mathrm{in}}(N_1,1)}, \ldots, e^{-j2\pi D^{\mathrm{in}}(N_1,N_2)}\Big]^T, \quad (11b)$$

where $D_k^{\mathrm{re}}(n_1, n_2)$ and $D^{\mathrm{in}}(n_1, n_2)$ denote the distance from the (n_1, n_2)-th[2] element of the XL-RIS to the kth user and the BS, respectively.

We can find that the main difference between the near-field channel $\bar{\mathbf{h}}_{\mathrm{NF},k}$ in (10) and the far-field channel $\bar{\mathbf{h}}_{\mathrm{FF},k}$ in (7) is the steering vector $\mathbf{b}(\cdot)$. Specifically, the far-field steering vector $\mathbf{b}(\phi, \varphi)$ is derived under the planar wavefront assumption, i.e., the steering vector is only related to the angles between the XL-RIS and the users (or BS). However, the steering vector $\mathbf{b}(\mathbf{r}_{\mathrm{re},k})$ (or $\mathbf{b}(\mathbf{r}_{\mathrm{in}})$) in the near-field is related to not only the angles but also the distances, since $\mathbf{r}_{\mathrm{re},k}$ (or $\mathbf{r}_{\mathrm{in}}$) is a directed vector.

Considering the fundamental difference between (7) and (10), the existing far-field codebooks (e.g., the discrete Fourier transformation (DFT) codebook[3]) designed for far-field beam training is no longer applicable. A hierarchical near-field codebook and corresponding hierarchical near-field beam training scheme have been proposed recently [26]. However, it will involve a serious performance loss if we directly utilize this codebook in the multi-user scenario because of the presence of constant modulus constraint for XL-RIS. To solve this problem, we propose a multi-beam design method, which will be discussed in the next section.

III. Proposed Multi-Beam Design Method

In this section, we devise the multi-beam design method for the XL-RIS aided wireless communications to design the passive beamforming vector. This method is composed of a beam training procedure and a multi-beam design procedure.

Intuitively, we draw Fig. 4 to show this the process for beam design with this method and data transmission over time. Specifically, the first procedure is executed by all users independently to acquire the desired single-beam direction of each user with a desired beam gain. Then, according to these beam parameters, the beamforming vector for XL-RIS will be designed in the multi-beam design procedure. Finally, this beamforming vector will be utilized for the data transmission.

[2]It means that this is the element located in the n_1th line and n_2th column of XL-RIS.

[3]As a widely adopted codebook, the definition and design approach for the DFT codebook can be studied as [38].

A. The Beam Training Procedure

As mentioned in Section I, by utilizing beam training, we do not need to acquire the accurate CSI by channel estimation [39] to design the RIS beamforming. Instead, we can directly determine the RIS beamforming vector via the beam training procedure. Firstly, the BS sends the training signals to the user via the RIS. This stage consists of several frames. During different frames, the RIS beamforming is configured according to different codewords of a pre-designed codebook $\mathcal{C}$ [26]. Secondly, the user will measure the power of received signals of different frames. Then, the desired codeword will be chosen according to the largest received power. Finally, this choice will be fed back to the BS via the uplink transmission, and the beamforming vector of the XL-RIS for data transmission will be determined as this codeword. The beam training procedure can be modeled as acquiring the desired RIS beamforming $\boldsymbol{\theta}$ satisfying

$$\boldsymbol{\theta} = \arg\max_{\mathbf{c}_i \in \mathcal{C}} \left| \bar{\mathbf{h}}_{\mathrm{NF}}^T \mathbf{c}_i \right|, \quad (12)$$

where $\bar{\mathbf{h}}_{\mathrm{NF}}$ is the near-field reflecting channel, and $\mathbf{c}_i$ is the codeword[4] for RIS beamforming selected from $\mathcal{C}$.

For the multi-user case, this procedure can be performed sequentially, based on which we can acquire the RIS beamforming for the kth user as $\boldsymbol{\theta}_k$. However, due to the constant modulus constraint for XL-RIS, serious loss for quality of service will be introduced if we can directly superpose these beamforming vectors. Our work [26] can support the beam training procedure in this paper. We focus on the challenging multi-beam design procedure in the next subsection to handle the influence of constant modulus constraint.

B. Multi-Beam Design Procedure

Considering that the near-field channel is related to angle information as well as distance information, the near-field codebook grids S is usually pretty large, based on which it will bring higher computational complexity for the multi-beam design. Note that compared with the beam gains in each grids for the whole space, we care more about the beam gains pointing to the K users' positions. Hence, in the proposed the near-field *multi-beam* design procedure, only the practical performance of K beams pointing to the K users are considered. Specifically, the multi-beam optimization problem can be expressed as

$$\mathcal{P}_{NF}: \min_{\boldsymbol{\theta}} \; l_1 = \left\| \bar{\mathbf{g}} - \boldsymbol{\Xi}^H \boldsymbol{\theta} \right\|_2^2 \quad \text{s.t.} \;\; \mathrm{C}: |\theta_n| = 1, \forall n \in \mathcal{N}, \quad (13)$$

where the XL-RIS beamforming vector $\boldsymbol{\theta}$ is the variable to be optimized and $\boldsymbol{\Xi} \in \mathbb{C}^{N \times K}$ is a steering matrix. $\boldsymbol{\Xi}$ consists of K columns, where the kth column is the codeword $\boldsymbol{\theta}_k$ acquired by beam training procedure. $\bar{\mathbf{g}} \in \mathbb{C}^{K \times 1}$ is the beam gains vector, and the corresponding elementwise amplitudes of $\bar{\mathbf{g}}$ are the desired beam gains for the K desired directions. This

[4]We can write a codebook $\mathcal{C}$ by a matrix form as $\mathbf{C} \in \mathbb{C}^{N \times S}$, where S is the codebook size, and codeword $\mathbf{c}_i$ is the ith column of this matrix.

objective function of $\mathcal{P}_{NF}$ can be rewritten as

$$l_1 = \bar{\mathbf{g}}^H \bar{\mathbf{g}} + \boldsymbol{\theta}^H \boldsymbol{\Xi}\boldsymbol{\Xi}^H \boldsymbol{\theta} - 2\mathrm{Re}\Big\{\bar{\mathbf{g}}^H \boldsymbol{\Xi}^H \boldsymbol{\theta}\Big\}. \tag{14}$$

With the fact that the number of users is usually smaller than the number of XL-RIS elements ($K < N$), the matrix $\boldsymbol{\Xi}\boldsymbol{\Xi}^H$ is an degenerate-rank matrix, i.e., we have $\boldsymbol{\Xi}\boldsymbol{\Xi}^H \neq \mathbf{I}_N$. As a result, $\mathcal{P}_{NF}$ is a non-convex quadratic programming problem, which is difficult to be solved.

In this paper, we propose a block coordinate descent (BCD) based scheme with majorization-minimization (MM) algorithm to solve this problem. The basic idea of the proposed scheme can be summarized as two aspects. Firstly, by utilizing the MM algorithm, we tackle the intractable problem by decomposing it to a series of sub-problems, which are tractable and can be iteratively solved to approach the optimal solution of the original problem. Secondly, we introduce the phase factors for multi-beam gains as extra optimizable variables. Thus, the degree of freedom of optimization can be enriched. Finally, the multiple beams can be designed by alternately optimizing the above two aspects with the BCD strategy.

1) Optimization for the Beamforming Vector: We adopt the MM algorithm to solve the problem $\tilde{\mathcal{P}}_{NF}$ to acquire the optimization of $\boldsymbol{\theta}$. The basic idea of the MM algorithm can be expressed as follows. For a difficult non-convex problem, we tackle it by dividing it to a series of approximate sub-problems, which are more tractable [40]. To iteratively solve these sub-problems in sequence, we can approach the optimal solution of the original objective function. Each iterative optimization is corresponding to a sub-problem.

Specifically, for a optimization problem $\min_{\boldsymbol{x}} f(\boldsymbol{x})$ subjecting to $\boldsymbol{x} \in \mathcal{X}$, a serious proxy functions $\{q(\boldsymbol{x}|\boldsymbol{x}^t)\}$, $(t = 1, 2, \ldots)$ will be constructed according to the MM algorithm. Each proxy function can be treated as the objective function of the sub-problem. $q(\boldsymbol{x}|\boldsymbol{x}^t)$ is objective function for the t+1th iteration, and we denote $\boldsymbol{x}^{t+1} = \arg\min_{\boldsymbol{x}} q(\boldsymbol{x}|\boldsymbol{x}^t)$. To solve the original problem, it is important to appropriately design the proxy functions $\{q(\boldsymbol{x}|\boldsymbol{x}^t)\}$. Taking the t + 1th iteration as an example, $q(\boldsymbol{x}|\boldsymbol{x}^t)$ is fulfilled the following four features as

$$f(\boldsymbol{x}) \leq q\big(\boldsymbol{x} \mid \boldsymbol{x}^t\big), \forall \boldsymbol{x} \in \mathcal{X}, \tag{15a}$$
$$f(\boldsymbol{x}) = q\big(\boldsymbol{x} \mid \boldsymbol{x}^t\big) \leftrightarrow \boldsymbol{x} = \boldsymbol{x}^t, \tag{15b}$$
$$\nabla_{\boldsymbol{x}} f(\boldsymbol{x})|_{\boldsymbol{x}=\boldsymbol{x}^t} = \nabla_{\boldsymbol{x}} q\big(\boldsymbol{x} \mid \boldsymbol{x}^t\big)\big|_{\boldsymbol{x}=\boldsymbol{x}^t}, \tag{15c}$$
$$q\Big(\boldsymbol{x}^{t+1}|\boldsymbol{x}^t\Big) = \min q\big(\boldsymbol{x}|\boldsymbol{x}^t\big) \leftrightarrow \boldsymbol{x} = \boldsymbol{x}^{t+1}. \tag{15d}$$

The first feature in (15a) ensures that each proxy function is the upper bound of the original objective function. The second and third features in (15b) and (15c) mean that in the unique intersection point, the first-order gradient should be equal between the original objective function and the proxy function. On this basis, it can be guaranteed with the last feature in (15d) that this upper bound is strictly decreasing from the tth iteration to the t + 1th iteration, based on which we have $f(\boldsymbol{x}^{t+1}) = q(\boldsymbol{x}^{t+1} \mid \boldsymbol{x}^t) \leq q(\boldsymbol{x}^t \mid \boldsymbol{x}^t) = f(\boldsymbol{x}^t)$.

By solving the sub-problems

$$\mathcal{P}_t: \min_{\boldsymbol{x}} \; q\big(\boldsymbol{x} \mid \boldsymbol{x}^t\big) \quad \text{s.t. C}: \; \boldsymbol{x} \in \mathcal{X}, \tag{16}$$

corresponding to the sequences of $\{q(\boldsymbol{x}|\boldsymbol{x}^t)\}$, $(t = 1, 2, \ldots)$, the optimal values of $\mathcal{P}_t$ is monotonically decreasing about t and finally converges to the optimal value of original problem.

Hence, for the difficult original objective function in (13), the core task is to design a suitable proxy function $\{q(\boldsymbol{x}|\boldsymbol{x}^t)\}$, which is much easier to be tackled than (13) and meeting the above four features. For convenience to discuss this issue, the optimization problem can be re-formulated according to (14) as

$$\mathcal{P}_{NF}: \min_{\boldsymbol{\theta}} \; l = \boldsymbol{\theta}^H \boldsymbol{\Xi}\boldsymbol{\Xi}^H \boldsymbol{\theta} - 2\mathrm{Re}\Big\{\bar{\mathbf{g}}^H \boldsymbol{\Xi}^H \boldsymbol{\theta}\Big\} \tag{17a}$$
$$\text{s.t. C}: |\theta_n| = 1, \forall n \in \mathcal{N}. \tag{17b}$$

Then, we give the **Lemma 1** as the effective strategy for designing $q(\boldsymbol{\theta}|\boldsymbol{\theta}^t)$ to optimize $\boldsymbol{\theta}$ in the t + 1th iteration.

Lemma 1: The proxy function $q(\boldsymbol{\theta}|\boldsymbol{\theta}^t)$ fulfilling the above four features can be defined as (18) at the bottom of the page for any given $\boldsymbol{\theta}^t$ and any available $\boldsymbol{\theta}$, where $\mathbf{M} \triangleq \lambda_{\max}\mathbf{I}_{N\times N}$ with $\lambda_{\max}$ denotes the maximum eigenvalue of $\boldsymbol{\Xi}\boldsymbol{\Xi}^H$.

Proof: See Appendix. ■

With the guidance from **Lemma 1**, the RIS beamforming $\boldsymbol{\theta}$ can be optimized by a iterative procedure to solve the minimization with a serious of $\{q(\boldsymbol{\theta}|\boldsymbol{\theta}^t)\}, (t = 1, 2, \ldots)$ according to (15) and (16). Specifically, for t + 1th iteration, by substituting $\mathbf{M}$ as $\lambda_{\max}\mathbf{I}_{N\times N}$, the optimization can be expressed as

$$\boldsymbol{\theta}^{t+1} = \exp\Big(j\angle\Big(\boldsymbol{\Xi}\bar{\mathbf{g}} - \boldsymbol{\Xi}\boldsymbol{\Xi}^H\boldsymbol{\theta}^t + \lambda_{\max}\boldsymbol{\theta}^t\Big)\Big). \tag{19}$$

2) Optimization for the Phase Factor: The constant modulus constraint results in the incomplete solution space of beam optimization. Hence, we introduce the phases for multi-beam gains an extra optimizable variables to enrich the degree of freedom of optimization objective. Specifically, we introduce the phase factor $\boldsymbol{\varpi} = [e^{j\zeta_1}, e^{j\zeta_2}, \ldots, e^{j\zeta_K}]$ of desired beam gains as the optimizable variable. This will not change the optimization goal, since the desired beam gain is only corresponding to the elementwise amplitude of $\bar{\mathbf{g}}$, i.e., $\tilde{\mathbf{g}} \in \mathbb{R}^{K\times 1}$. By denoting $\bar{\mathbf{g}} = \tilde{\mathbf{g}} \odot \boldsymbol{\varpi}$, (17) can be expressed as

$$\tilde{\mathcal{P}}_{NF}: \min_{\boldsymbol{\theta},\boldsymbol{\varpi}} \; l = \boldsymbol{\theta}^H \boldsymbol{\Xi}\boldsymbol{\Xi}^H \boldsymbol{\theta} - 2\mathrm{Re}\Big\{(\tilde{\mathbf{g}} \odot \boldsymbol{\varpi})^H \boldsymbol{\Xi}^H \boldsymbol{\theta}\Big\} \tag{20a}$$
$$\text{s.t. C}_1: |\theta_n| = 1, \forall n \in \mathcal{N}, \tag{20b}$$
$$\text{C}_2: \varpi_k = e^{j\zeta_k}, \forall k \in \mathcal{K}, \zeta_k \in [0, 2\pi]. \tag{20c}$$

For a given $\boldsymbol{\theta}^t$, the phase factor $\boldsymbol{\varpi}$ can be optimized as

$$\boldsymbol{\varpi} = \exp\Big(j\angle\Big(\boldsymbol{\Xi}^H\boldsymbol{\theta}^t\Big)\Big). \tag{21}$$

$$l = \boldsymbol{\theta}^H \boldsymbol{\Xi}\boldsymbol{\Xi}^H \boldsymbol{\theta} - 2\mathrm{Re}\big\{\bar{\mathbf{g}}^H \boldsymbol{\Xi}^H \boldsymbol{\theta}\big\} \leq q\big(\boldsymbol{\theta}|\boldsymbol{\theta}^t\big) \triangleq \boldsymbol{\theta}^H \mathbf{M}\boldsymbol{\theta} + 2\mathrm{Re}\Big\{\boldsymbol{\theta}^H\big(\boldsymbol{\Xi}\boldsymbol{\Xi}^H - \mathbf{M}\big)\boldsymbol{\theta}^t\Big\} + \boldsymbol{\theta}^{tH}(\mathbf{M} - \boldsymbol{\Xi}\boldsymbol{\Xi}^H)\boldsymbol{\theta}^t - 2\mathrm{Re}\{\bar{\mathbf{g}}^H \boldsymbol{\Xi}^H \boldsymbol{\theta}\}, \tag{18}$$

Algorithm 1 BCD-Based Multi-Beams Design Procedure

Input: Desired beam gain $\tilde{\mathbf{g}}$, maximum eigenvalue $\lambda_{\max}$, desirable accuracy ϵ, allowable threshold μ, maximum iteration $t_{\max}$, steering matrix $\boldsymbol{\Xi}$.

Output: Optimized beamforming vector $\boldsymbol{\theta}^{\text{opt}}$.

Init. initialized phase factor $\boldsymbol{\varpi}^{(0)}$, initialized beamforming vector $\boldsymbol{\theta}^{(0)}$, $i = 0$.
while $\left\|\bar{\mathbf{g}}^{(i)} - \boldsymbol{\Xi}^H \boldsymbol{\theta}^{(i)}\right\|_2^2 \geq \epsilon$ **do**
  $\boldsymbol{\varpi}^{(i+1)} = \exp(j\angle(\boldsymbol{\Xi}^H \boldsymbol{\theta}^{(i)}))$.
  $\bar{\mathbf{g}}^{(i+1)} = \tilde{\mathbf{g}} \odot \boldsymbol{\varpi}^{(i+1)}$.
  $\boldsymbol{\theta}^t|_{t=1} = \boldsymbol{\theta}^{(i)}$.
  for $t = 1$ **to** $t = t_{\max}$ **do**
    $\boldsymbol{\theta}^{t+1} = \exp(j\angle(\boldsymbol{\Xi}(\tilde{\mathbf{g}} \odot \boldsymbol{\varpi}^{(i+1)}) - \boldsymbol{\Xi}\boldsymbol{\Xi}^H \boldsymbol{\theta}^t + \lambda_{\max}\boldsymbol{\theta}^t))$.
    if $|\boldsymbol{\theta}^{t+1} - \boldsymbol{\theta}^t| < \mu$ **then**
      $\boldsymbol{\theta}^{(i+1)} = \boldsymbol{\theta}^{t+1}$.
      Break.
    else if $t = t_{\max}$ **then**
      $\boldsymbol{\theta}^{(i+1)} = \boldsymbol{\theta}^{t_{\max}+1}$.
      Break.
    else
      $t = t + 1$.
    end if
  end for
  $i = i + 1$.
end while
$\boldsymbol{\theta}^{\text{opt}} = \boldsymbol{\theta}^{(i)}$.

According to the above two steps, the variable $\boldsymbol{\theta}$ and $\boldsymbol{\varpi}$ can be alternately optimized with the BCD strategy. For clarity, we summarize the whole process of this proposed BCD-based multi-beam design in **Algorithm 1**, based on which we can acquire the solution for RIS beamforming as $\boldsymbol{\theta}^{\text{opt}}$.

C. Complexity Analysis

The complexity for the proposed scheme can be expressed as two parts. Firstly, considering that each step of optimization procedure can be expressed as corresponding closed-form solution, the calculation complexity for the closed-form solution for $\boldsymbol{\theta}$ and $\boldsymbol{\varpi}$ can be expressed as $\mathcal{O}(LKN^2)$, with L as the iteration times. The second part is for calculating the eigenvalue of $\boldsymbol{\Xi}\boldsymbol{\Xi}^H$, which can be expressed as $\mathcal{O}(N^3)$. Since we usually have $K \ll N$, the complexity of the proposed scheme is mainly depends on $\mathcal{O}(N^3)$, which seems intractable. For this issue, we give Proposition 1 as a straightforward trick, based on which the complexity for acquiring the $\lambda_{\max}$ in our proposed scheme can be significantly reduced to $\mathcal{O}(K^3)$ rather than $\mathcal{O}(N^3)$, where we usually have $K \ll N$.

Proposition 1: The calculation for $\lambda_{\max}$ is with the equivalent to acquire the maximum eigenvalue of the K-dimension square matrix $\mathbf{T} \in \mathbb{C}^{K\times K}$, if we have $\mathbf{T} = \boldsymbol{\Xi}^H\boldsymbol{\Xi}$.

Proof: By utilizing the singular value decomposition (SVD), we can expressed $\boldsymbol{\Xi} \in \mathbb{C}^{N\times K}$ as $\boldsymbol{\Xi} = \boldsymbol{U}\boldsymbol{\Sigma}\boldsymbol{V}^H$. $\boldsymbol{U} \in \mathbb{C}^{N\times N}$, and $\boldsymbol{V} \in \mathbb{C}^{K\times K}$ are the unitary matrix. $\boldsymbol{\Sigma} \in \mathbb{C}^{N\times K}$ is the singular value matrix which can be expressed as $\boldsymbol{\Sigma} = [\tilde{\boldsymbol{\Sigma}}, \boldsymbol{O}]^T$, where $\boldsymbol{O} \in \mathbb{C}^{(N-K)\times K}$ is a null matrix, and the $\tilde{\boldsymbol{\Sigma}}$ can be expressed as a diagonal matrix with K singular values on its diagonal, i.e.,

$$\tilde{\boldsymbol{\Sigma}} = \text{diag}(\kappa_{\max}, \ldots, \kappa_i, \ldots, \kappa_{\min}), \tag{22}$$

where $\kappa_{\max}$ is the maximum singular value of $\boldsymbol{\Xi}$.

Note that $\boldsymbol{\Xi}\boldsymbol{\Xi}^H = \boldsymbol{U}\boldsymbol{\Sigma}\boldsymbol{\Sigma}^H\boldsymbol{U}^H \triangleq \boldsymbol{U}\boldsymbol{\Lambda}\boldsymbol{U}^{-1}$. According to the definition for eigenvalue, the maximum eigenvalue $\lambda_{\max}$ can be calculated as $\kappa_{\max}^2$.

Similarly, the maximum eigenvalue for $\mathbf{T} = \boldsymbol{V}\boldsymbol{\Sigma}^H\boldsymbol{\Sigma}\boldsymbol{V}^H \triangleq \boldsymbol{V}\boldsymbol{\Lambda}^T\boldsymbol{V}^{-1}$ is equal to $\kappa_{\max}^2$. Hence, we can calculate $\lambda_{\max}$ via the eigenvalue decomposition for K-dimension matrix $\mathbf{T}$ with complexity as only $\mathcal{O}(K^3)$. ■

With the method of Proposition 1, the computational complexity for the proposed scheme can be expressed as $\mathcal{O}(LKN^2) + \mathcal{O}(K^3)$ rather than $\mathcal{O}(LKN^2) + \mathcal{O}(N^3)$.

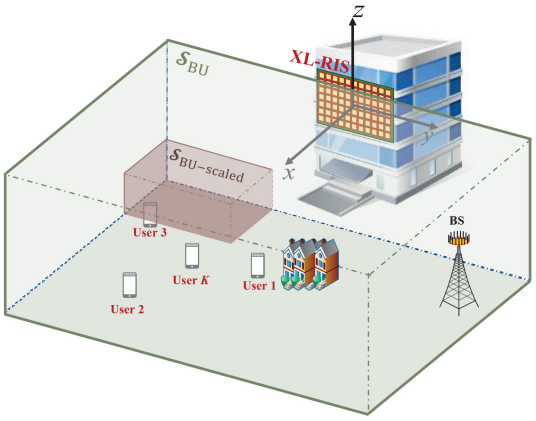

Fig. 5. An illustration of the simulation scenario, where the XL-RIS center locates at origin of coordinates. The BS and users are randomly distributed in the space $\mathcal{S}_{\text{AD}}$.

IV. Simulation Results

We discuss the simulation results of the proposed multi-beam design in the XL-RIS aided near-field wireless communications in this section. Besides, the performance is also discussed in the far-field scenario, based on which the universality of the proposed scheme can be verified.

A. Simulation Setup

1) Simulation Scenario: We consider a three-dimensional scenario with the topology in the Cartesian coordinate system as shown in Fig. 5, where the XL-RIS is deployed on the yOz-plane with its center located at the origin of coordinate (0, 0, 0), i.e., the region for the XL-RIS in the coordinate system can be expressed as

$$\mathcal{S}_{\text{R}} \coloneqq \left\{ (s_x, s_y, s_z) \middle| |s_x| = 0, |s_y| \leq \frac{L_y}{2}, |s_z| \leq \frac{L_z}{2} \right\}, \tag{23}$$

where L_y and L_z are the width and height of XL-RIS. For the uniform array XL-RIS with $d_R = \lambda/2$, we have $L_y = N_1\lambda/2$ and $L_z = N_2\lambda/2$. Considering that the BS and users are randomly distributed in the 3-D space, as the green region in Fig. 5, where the region can be expressed as

$$\mathcal{S}_{\text{BU}} \coloneqq \left\{ (s_x, s_y, s_z) \middle| s_x \in \mathcal{R}_x, s_y \in \mathcal{R}_y, s_z \in \mathcal{R}_z \right\}, \tag{24}$$

TABLE I
SIMULATION PARAMETERS SETUP FOR THE NEAR-FIELD SCENARIO

Parameters	Value
Numbers of XL-RIS elements (hori.)	$N_1 = 64$
Numbers of XL-RIS elements (vert.)	$N_2 = 8$
Carrier frequency	$f = 10$ GHz
Wavelength	$\lambda = 0.03$ m
Element spacing for XL-RIS	$d_R = \lambda/2$
Number of users	$K \in [2, 20]$
Width of XL-RIS	$L_y = 0.12$ m
Height of XL-RIS	$L_z = 0.96$ m
Aperture of XL-RIS	$D_{\text{RIS}} = \text{sqrt}(L_y^2 + L_z^2)$
Coordinate for the XL-RIS center	$(0, 0, 0)$
Region for BS & users distribution	$\mathcal{R}_x = [200d_R, 1200d_R]$
Region for BS & users distribution	$\mathcal{R}_y = [-2500d_R, 2500d_R]$
Region for BS & users distribution	$\mathcal{R}_z = [-1000d_R, 0]$
SNR	$SNR \in [-10, 5]$ dB
Distance between user & XL-RIS	$r \in [3, 44]$ m
Rayleigh distance	$R = 62.4$ m
Density factor	$\rho \in [0, 0.7]$

where $\mathcal{R}_x = [R_{x,\min}, R_{x,\max}]$, $\mathcal{R}_y = [R_{y,\min}, R_{y,\max}]$, and $\mathcal{R}_z = [R_{z,\min}, R_{z,\max}]$, respectively. For the convenience to flexibly change the density of the users distribution, we introduce a density factor ρ to scale the available region for users distribution as

$$\mathcal{S}_{\text{BU}-\text{scaled}} \coloneqq \left\{ \left(s_x, s_y, s_z\right) \middle| s_x \in \mathcal{R}'_x, s_y \in \mathcal{R}'_y, s_z \in \mathcal{R}'_z \right\}, \tag{25}$$

where we denote

$$\mathcal{R}'_x = \left[R_{x,\min}, R_{x,\max} - \rho\left(R_{x,\max} - R_{x,\min}\right)\right], \tag{26}$$

same goes for $\mathcal{R}'_y$ and $\mathcal{R}'_z$. Hence, we can shrink the available region for users distribution by increasing the factor ρ, based on which users will be more closely distributed, as the red region in Fig. 5.

2) Simulation Parameters: The simulation parameters for the near-field scenario are determined following Table I. Note that the Rayleigh distance in this scenario can be calculated as $R = 2D_{\text{RIS}}^2/\lambda = 62.4$ m, and the distance between the center of XL-RIS and the user (or BS) is from 3 m to 44 m, i.e., all users and the BS in $\mathcal{S}_{\text{BU}}$ are located in the near-field region of XL-RIS.

3) Simulation Baselines: We consider the existing near-field codebook based single-beam design (NF-based single-beam design) [26] and the far-field (DFT) codebook based single-beam design (FF-based single-beam design). To serve multiple users, these two single-beam design schemes superpose the beam design codewords for all users as the effective beamforming vector.

B. Simulation Results

From Fig. 6 to Fig. 8, we discuss the performance gain for the proposed scheme compared with the simulation baselines. By considering the quality of service, we choose the minimal rate as the performance indicator, which refers to the minimum one for achievable rates of all users.

Fig. 6 illustrates the minimal rate against the number of users. The received signal-to-noise ratio (SNR) is set as 5 dB, and the density factor ρ is set as 0, i.e., users and BS are distributed in the whole region of $\mathcal{S}_{\text{AD}}$. From Fig. 6 we can find

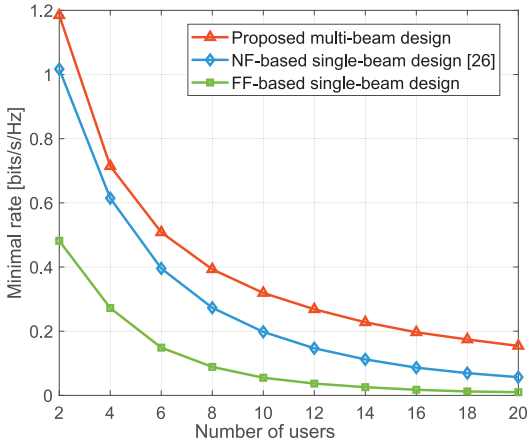

Fig. 6. Minimal rate performance comparison against the number of users.

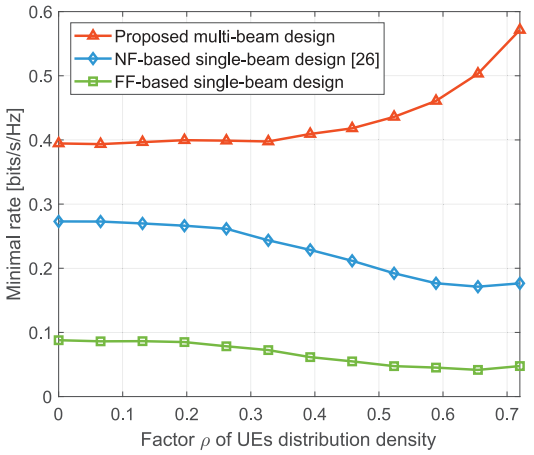

Fig. 7. Minimal rate performance comparison against the density factor ρ of users distribution.

that the minimal rate of proposed beam design is superior to the existing hierarchical near-field codebook based (NF-based) single-beam design [26] and the far-field codebook (i.e., DFT codebook) based (FF-based) single-beam design. To serve multiple users, these single-beam design schemes have to superpose the beam design codewords for each users as effective beamforming vector. Note that with the increasing number of users, despite the rates decreased due to the limitation for transmitted power, the proposed scheme still has an advantaged performance. For example, with $K = 10$, the minimal rate for the proposed scheme is more than 80% compared with the NF-based single-beam scheme.

In addition, we are also concerned about the performance when users are located in a compact range (i.e., the $\mathcal{S}_{\text{AD}-\text{scaled}}$ region). The minimal rate performance with respect to density factor ρ of users distribution is evaluated in Fig. 7. With the increasing of ρ, the region of users distribution will be shrunk from $\mathcal{S}_{\text{AD}}$ to $\mathcal{S}_{\text{AD}-\text{scaled}}$ according to Fig. 5 and (26), i.e., in this scenario users will be distributed more narrowed. The SNR is set as 5 dB, and K is set as 8. From Fig. 7 we can find that with the increase for density factor, the minimal rate for the proposed multi-beam design scheme is superior to the existing single-beam design. Besides, since

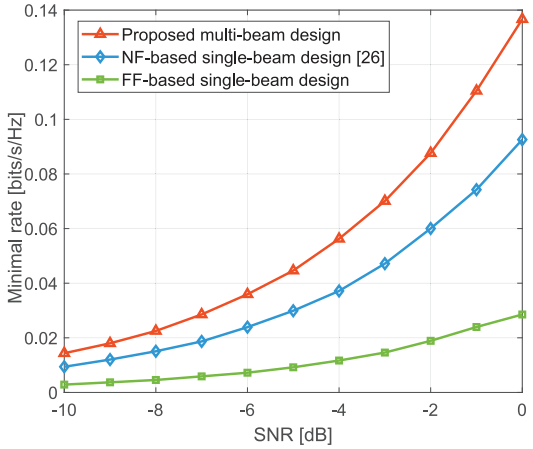

Fig. 8. Minimal rate performance comparison against the SNR.

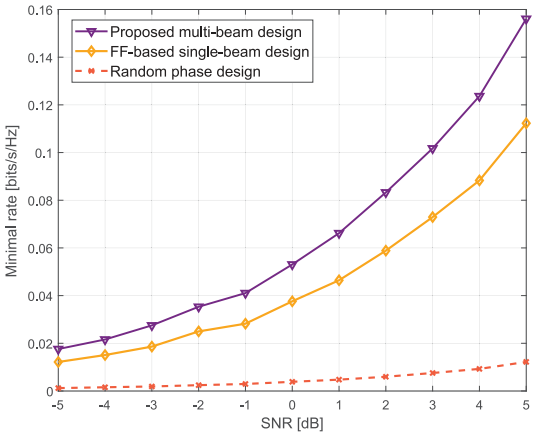

Fig. 9. Minimal rate performance comparison against the SNR in the far-field scenario.

the orthogonality of the codeword for the adjacent users is worse, the beam direction for the NF-based single-beam design will deviate from the desired direction, as a consequence, the performance will be limited.

Fig. 8 compares minimal rate performance against SNR. The number of users K is set as 8, and the density factor ρ is set as 0, i.e., users and BS are randomly distributed in the whole near-field region $\mathcal{S}_{\mathrm{AD}}$. Fig. 8 shows that the minimal rate for the proposed scheme is better than the NF-based or the FF-based single-beam design in different SNRs. For example, in the scenario with SNR as 0 dB, the minimal rate for the proposed scheme is 50% higher than the NF-based single-beam scheme. Due to the fundamental difference between the near-field propagation and far-field propagation, this performance for the proposed scheme is 300% higher than the far-field scheme.

C. An Extended Discussion in the Far-Field Scenario

To ensure that the proposed scheme is also feasible in the far-field scenario, we also discuss our proposed scheme for far-field channel, which has been studied extensively under the Saleh-Valenzuela channel model [7] in (5).

In Fig. 9, we consider the far-field scenario with the RIS deploying 16 elements ($N = 16$) to serve 6 users ($K = 6$) simultaneously. The DFT codebook is adopted as the far-field codebook. The result in Fig. 9 illustrates that in the far-field scenario, the proposed scheme still has a performance advantage compared with the existing single-beam design. Besides, note that compared with the XL-RIS scenario, the minimal rate of Fig. 9 is lower than the Fig. 8. For example, with SNR as 0 dB, the minimal rate for the proposed scheme is 0.14 bits/s/Hz in Fig. 8 while it is only 0.05 bits/s/Hz in Fig. 9. This is mainly because under the same condition (e.g., the same transmitted power and the SNR) the XL-RIS with more elements can provide higher RIS beamforming gain compared with the RIS, which results in a significant performance gain.

Then, in the following part, we discuss the proposed scheme from the perspective of beam gain. In Fig. 10, we consider that the RIS still transmits 6 beams in different directions. For convenience, we discuss the azimuth spatial angle within the range

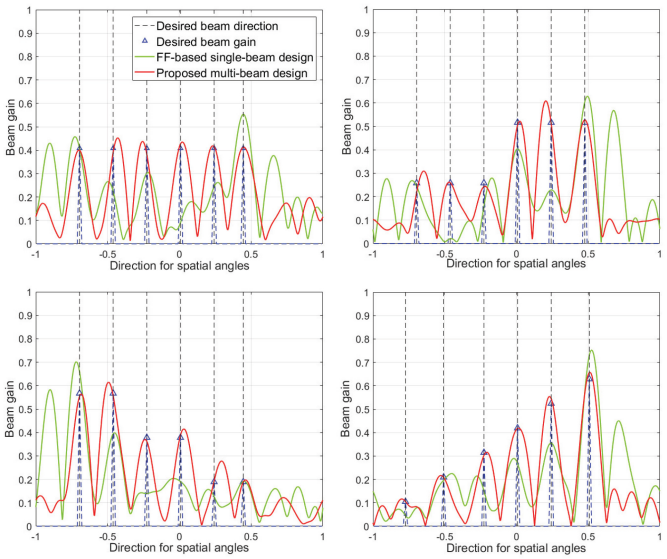

Fig. 10. The beam gains for equipower and unequal power multi-beam design.

of $[-1, 1]$.[5] In every sub-figure of Fig. 10, the X-coordinates for the six triangles represent the desired directions of the six beams, while the Y-coordinates represent the desired beam gains. We consider the equipower multi-beam design, and the unequal power multi-beam design. Specifically, we consider four conditions about the desired gains for the multiple beams in the four sub-figures:

1) equipower scenario: $P_1, P_2, \ldots, P_6 = p, p, p, p, p, p$,
2) unequal power: $P_1, \ldots, P_6 = p, p, p, 2p, 2p, 2p$,
3) unequal power: $P_1, \ldots, P_6 = 3p, 3p, 2p, 2p, p, p$,
4) unequal power: $P_1, \ldots, P_6 = p, 2p, 3p, 4p, 5p, 6p$.

Fig. 10 shows that both in the equipower multi-beam design, and the unequal power multi-beam design, the proposed scheme can provide multi-beams pointing to the desired directions with desired beam gain. As a contrast, the performance of FF-based single-beam design is accompanied by the offset in the direction and the error in the beam gain.

[5]Actually, the range of $\phi_{\mathrm{re},k}$ is $[-1/2, 1/2]$ with considering $d_R/\lambda = 1/2$, and the range of $e^{j2\pi\phi_{\mathrm{re},k}}$ is $[-1, 1]$, which is the x-axis of Fig. 10.

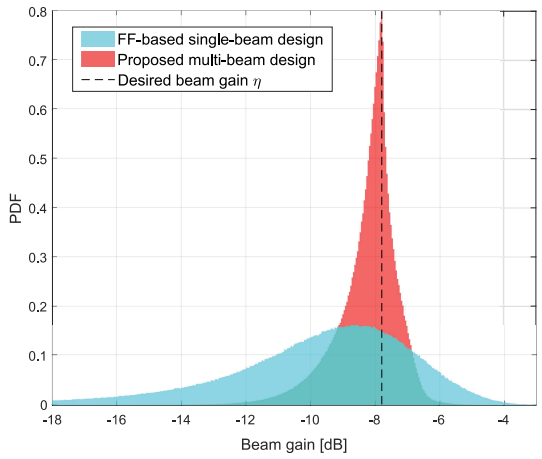

Fig. 11. The probability density function figure about the beam gains in random directions.

Finally, we provide a probability density function (PDF) figure as Fig. 11 after 500,000 times simulations. In every simulation, the desired directions for spatial angles of the six beams are randomly selected. Assuming the beam gain in the single-beam scenario is 0 dB, then the equivalent beam gain for the multi-beam scenario can be calculated as $\eta = 10 \times \log_{10} 1/6 = -7.8$ dB in the equipower scenario, as shown in Fig. 11. We can exploit that, compared with the single-beam design, the PDF for the proposed scheme is significantly better, based on which we can know that when we design the beam pointing to different directions, the proposed scheme is superior to the single-beam design with higher accuracy and more ideal gain in a statistical sense.

V. Conclusion

In this paper, we have investigated the near-field multi-beam design method for XL-RIS aided wireless communications to serve multiple users. Most of the existing works for near-field RIS systems focused on the single-beam design. However, a serious performance loss will be brought if we directly utilize these existing schemes in multi-user case, due to the presence of constant modulus constraint. To overcome this constraint, we have proposed a BCD-based scheme with the MM algorithm for the multi-beam design. Simulation results have shown that the proposed multi-beam design could achieve a superior quality of service 50% higher than the conventional schemes. Particularly, the proposed scheme also has a performance gain in the far-field scenario. Finally, for mobile users with high velocities, it is important to explore how to timely adjust the beams according to the movement of users. Hence, we leave the near-field beam tracking in RIS-aided wireless communications for future work.

Appendix

Proof of Lemma 1

To design $q(\boldsymbol{\theta}|\boldsymbol{\theta}^t)$, it is important to acquire the upper bound of the subjective function l. For this purpose, we exploit the second-order Taylor expansion for the subjective function at first. For a real-valued function $f(\boldsymbol{z}, \boldsymbol{z}^*)$ that takes complex values $(\boldsymbol{z}, \boldsymbol{z}^*)$ as arguments, the second-order series approximation via the second-order Taylor expansion in $(\boldsymbol{z}_0, \boldsymbol{z}_0^*)$ can be expressed as

$$f(\boldsymbol{z}, \boldsymbol{z}^*) \approx f(\boldsymbol{z}_0, \boldsymbol{z}_0^*) + (\nabla f(\boldsymbol{z}_0, \boldsymbol{z}_0^*))^{\mathrm{T}} \Delta\tilde{\boldsymbol{z}}_0 + \frac{1}{2}(\Delta\tilde{\boldsymbol{z}}_0)^H H(f(\boldsymbol{z}_0, \boldsymbol{z}_0^*))\Delta\tilde{\boldsymbol{z}}_0, \tag{27}$$

where $\Delta\tilde{\boldsymbol{z}}_0 = \begin{bmatrix} \Delta\boldsymbol{z}_0 \\ \Delta\boldsymbol{z}_0^* \end{bmatrix}$ with $\Delta\boldsymbol{z}_0 = \boldsymbol{z} - \boldsymbol{z}_0$ and $\Delta\boldsymbol{z}_0^* = \boldsymbol{z}^* - \boldsymbol{z}_0^*$; $\nabla f(\boldsymbol{z}_0, \boldsymbol{z}_0^*)$ is the gradient vector for $f(\boldsymbol{z}, \boldsymbol{z}^*)$, and $H(f(\boldsymbol{z}_0, \boldsymbol{z}_0^*))$ is the Hessian matrix. Then, (27) can be rewritten as

$$\begin{aligned} f(\boldsymbol{z}, \boldsymbol{z}^*) \approx\ & f(\boldsymbol{z}_0, \boldsymbol{z}_0^*) \\ & + \left[\frac{\partial f(\boldsymbol{z}_0, \boldsymbol{z}_0^*)}{\partial \boldsymbol{z}^T}, \frac{\partial f(\boldsymbol{z}_0, \boldsymbol{z}_0^*)}{\partial \boldsymbol{z}^H}\right] \begin{bmatrix} \Delta\boldsymbol{z}_0 \\ \Delta\boldsymbol{z}_0^* \end{bmatrix} \\ & + \frac{1}{2}\left[\Delta\boldsymbol{z}_0^H, \Delta\boldsymbol{z}_0^{\mathrm{T}}\right] \begin{bmatrix} \frac{\partial^2 f(\boldsymbol{z}_0, \boldsymbol{z}_0^*)}{\partial \boldsymbol{z}^* \partial \boldsymbol{z}^T} & \frac{\partial^2 f(\boldsymbol{z}_0, \boldsymbol{z}_0^*)}{\partial \boldsymbol{z}^* \partial \boldsymbol{z}^H} \\ \frac{\partial^2 f(\boldsymbol{z}_0, \boldsymbol{z}_0^*)}{\partial \boldsymbol{z} \partial \boldsymbol{z}^T} & \frac{\partial^2 f(\boldsymbol{z}_0, \boldsymbol{z}_0^*)}{\partial \boldsymbol{z} \partial \boldsymbol{z}^H} \end{bmatrix} \begin{bmatrix} \Delta\boldsymbol{z}_0 \\ \Delta\boldsymbol{z}_0^* \end{bmatrix}. \end{aligned} \tag{28}$$

We focus on the second-order Taylor expansion for $\boldsymbol{\theta}^H \boldsymbol{\Xi}\boldsymbol{\Xi}^H \boldsymbol{\theta}$. Lets denote $\boldsymbol{\Xi}\boldsymbol{\Xi}^H$ as $\mathbf{A}$, and $\boldsymbol{\theta}^H \boldsymbol{\Xi}\boldsymbol{\Xi}^H \boldsymbol{\theta}$ as $u(\boldsymbol{\theta}, \boldsymbol{\theta}^*) = \boldsymbol{\theta}^H \mathbf{A} \boldsymbol{\theta}$, based on which we calculate the first-order partial derivative vector and second-order partial derivative matrix of (28) as follows.

The first-order partial derivative vector $\frac{\partial u(\boldsymbol{\theta}, \boldsymbol{\theta}^*)}{\partial \boldsymbol{\theta}}$ can be expressed as

$$\frac{\partial u(\boldsymbol{\theta}, \boldsymbol{\theta}^*)}{\partial \boldsymbol{\theta}} = \frac{\partial}{\partial \boldsymbol{\theta}} \sum_{k=1}^{n} \sum_{l=1}^{n} \theta_k^* A_{kl} \theta_l = (\mathbf{A}\boldsymbol{\theta})^*, \tag{29}$$

where $A_{kl} = \mathbf{A}_{(k,l)}$, and $\theta = \boldsymbol{\theta}_{(k)}$. Similarly, $\frac{\partial u(\boldsymbol{\theta}, \boldsymbol{\theta}^*)}{\partial \boldsymbol{\theta}^*}$ can be calculated as

$$\frac{\partial u(\boldsymbol{\theta}, \boldsymbol{\theta}^*)}{\partial \boldsymbol{\theta}^*} = \frac{\partial}{\partial \boldsymbol{\theta}^*} \sum_{k=1}^{n} \sum_{l=1}^{n} \theta_k^* A_{kl} \theta_l = \mathbf{A}\boldsymbol{\theta}. \tag{30}$$

The second-order partial derivative matrix can be calculated as

$$\frac{\partial^2 u(\boldsymbol{\theta}, \boldsymbol{\theta}^*)}{\partial \boldsymbol{\theta}^* \partial \boldsymbol{\theta}^T} = \mathbf{A}, \tag{31a}$$

$$\frac{\partial^2 u(\boldsymbol{\theta}, \boldsymbol{\theta}^*)}{\partial \boldsymbol{\theta} \partial \boldsymbol{\theta}^H} = \mathbf{A}^*, \tag{31b}$$

$$\frac{\partial^2 u(\boldsymbol{\theta}, \boldsymbol{\theta}^*)}{\partial \boldsymbol{\theta} \partial \boldsymbol{\theta}^T} = \mathbf{O}, \tag{31c}$$

$$\frac{\partial^2 u(\boldsymbol{\theta}, \boldsymbol{\theta}^*)}{\partial \boldsymbol{\theta}^* \partial \boldsymbol{\theta}^H} = \mathbf{O}. \tag{31d}$$

Hence, the second-order Taylor expansion for $u(\boldsymbol{\theta}, \boldsymbol{\theta}^*)$ in $(\boldsymbol{\theta}^t, \boldsymbol{\theta}^{t*})$ according to (28) can be rewritten as

$$\begin{aligned} u(\boldsymbol{\theta}, \boldsymbol{\theta}^*) = {} & \boldsymbol{\theta}^{tH} \boldsymbol{\Xi}\boldsymbol{\Xi}^H \boldsymbol{\theta}^t + 2\mathrm{Re}\left\{\left(\boldsymbol{\theta} - \boldsymbol{\theta}^t\right)^H \boldsymbol{\Xi}\boldsymbol{\Xi}^H \boldsymbol{\theta}^t\right\} \\ & + \left(\boldsymbol{\theta} - \boldsymbol{\theta}^t\right)^H \boldsymbol{\Xi}\boldsymbol{\Xi}^H \left(\boldsymbol{\theta} - \boldsymbol{\theta}^t\right). \end{aligned} \tag{32}$$

Considering $\mathbf{M} \triangleq \lambda_{\max} \mathbf{I}_{N \times N}$ with $\lambda_{\max}$ denoting the maximum eigenvalue of $\boldsymbol{\Xi}\boldsymbol{\Xi}^H$, we have $\mathbf{M} - \boldsymbol{\Xi}\boldsymbol{\Xi}^H \succeq \mathbf{O}$. Thus,

we can relax the third item of Taylor expansion in (32) as $(\boldsymbol{\theta}-\boldsymbol{\theta}^t)^H\mathbf{M}(\boldsymbol{\theta}-\boldsymbol{\theta}^t)$, based on which the upper bound for $u(\boldsymbol{\theta},\boldsymbol{\theta}^*)$ can be calculated as

$$\begin{aligned} u(\boldsymbol{\theta},\boldsymbol{\theta}^*) &\le \boldsymbol{\theta}^{tH}\boldsymbol{\Xi}\boldsymbol{\Xi}^H\boldsymbol{\theta}^t + 2\mathrm{Re}\Big\{\left(\boldsymbol{\theta}-\boldsymbol{\theta}^t\right)^H\boldsymbol{\Xi}\boldsymbol{\Xi}^H\boldsymbol{\theta}^t\Big\} \\ &\quad + \left(\boldsymbol{\theta}-\boldsymbol{\theta}^t\right)^H\mathbf{M}\left(\boldsymbol{\theta}-\boldsymbol{\theta}^t\right) \\ &= \boldsymbol{\theta}^{t\,H}\Big(\mathbf{M}-\boldsymbol{\Xi}\boldsymbol{\Xi}^H\Big)\boldsymbol{\theta}^t \\ &\quad + 2\mathrm{Re}\Big\{\boldsymbol{\theta}^H\Big(\boldsymbol{\Xi}\boldsymbol{\Xi}^H-\mathbf{M}\Big)\boldsymbol{\theta}^t\Big\} + \boldsymbol{\theta}^H\mathbf{M}\boldsymbol{\theta}. \quad (33) \end{aligned}$$

Then, for the objective function $l = u(\boldsymbol{\theta},\boldsymbol{\theta}^*) + 2\mathrm{Re}\{\bar{\mathbf{g}}^H\boldsymbol{\Xi}^H\boldsymbol{\theta}\}$, the proxy function $q(\boldsymbol{\theta}|\boldsymbol{\theta}^t)$ can be represented as

$$\begin{aligned} q\left(\boldsymbol{\theta}|\boldsymbol{\theta}^t\right) &\triangleq \boldsymbol{\theta}^H\mathbf{M}\boldsymbol{\theta} + 2\mathrm{Re}\Big\{\boldsymbol{\theta}^H\Big(\boldsymbol{\Xi}\boldsymbol{\Xi}^H-\mathbf{M}\Big)\boldsymbol{\theta}^t\Big\} \\ &\quad + \boldsymbol{\theta}^{t\,H}\Big(\mathbf{M}-\boldsymbol{\Xi}\boldsymbol{\Xi}^H\Big)\boldsymbol{\theta}^t - 2\mathrm{Re}\Big\{\bar{\mathbf{g}}^H\boldsymbol{\Xi}^H\boldsymbol{\theta}\Big\}, \quad (34) \end{aligned}$$

which completes the proof of **Lemma 1**.

REFERENCES

[1] D. Shen and L. Dai, "Multi-beam design for extremely large-scale RIS aided near-field wireless communications," in *Proc. IEEE Global Commun. Conf. (IEEE GLOBECOM)*, Rio de Janeiro, Brazil, Dec. 2022, pp. 1–6.

[2] S. Ma, W. Shen, J. An, and L. Hanzo, "Wideband channel estimation for IRS-aided systems in the face of beam squint," *IEEE Trans. Wireless Commun.*, vol. 20, no. 10, pp. 6240–6253, Oct. 2021.

[3] Y. Chen, Y. Wang, J. Zhang, and M. D. Renzo, "QoS-driven spectrum sharing for reconfigurable intelligent surfaces (RISs) aided vehicular networks," *IEEE Trans. Wireless Commun.*, vol. 20, no. 9, pp. 5969–5985, Sep. 2021.

[4] S. Zhang, S. Zhang, F. Gao, J. Ma, and O. A. Dobre, "Deep learning optimized sparse antenna activation for reconfigurable intelligent surface assisted communication," *IEEE Trans. Commun.*, vol. 69, no. 10, pp. 6691–6705, Oct. 2021.

[5] M. Xu, S. Zhang, J. Ma, and O. A. Dobre, "Deep learning-based time-varying channel estimation for RIS assisted communication," *IEEE Commun. Lett.*, vol. 26, no. 1, pp. 94–98, Jan. 2022.

[6] C. Feng, W. Shen, J. An, and L. Hanzo, "Joint hybrid and passive RIS-assisted Beamforming for mmWave MIMO systems relying on dynamically configured subarrays," *IEEE Internet Things J.*, vol. 9, no. 15, pp. 13913–13926, Aug. 2022.

[7] S. Liu, Z. Gao, J. Zhang, M. D. Renzo, and M.-S. Alouini, "Deep denoising neural network assisted compressive channel estimation for mmWave intelligent reflecting surfaces," *IEEE Trans. Veh. Technol.*, vol. 69, no. 8, pp. 9223–9228, Aug. 2020.

[8] X. Pang, N. Zhao, J. Tang, C. Wu, D. Niyato, and K.-K. Wong, "IRS-assisted secure UAV transmission via joint trajectory and Beamforming design," *IEEE Trans. Commun.*, vol. 70, no. 2, pp. 1140–1152, Feb. 2022.

[9] W. Xu, L. Gan, and C. Huang, "A robust deep learning-based Beamforming design for RIS-assisted multiuser MISO communications with practical constraints," *IEEE Trans. Cogn. Commun. Netw.*, vol. 8, no. 2, pp. 694–706, Jun. 2022.

[10] Z. Wan, Z. Gao, and M.-S. Alouini, "Broadband channel estimation for intelligent reflecting surface aided mmWave massive MIMO systems," in *Proc. IEEE Int. Conf. Commun. (ICC'20)*, Dublin, Ireland, Jun. 2020, pp. 1–6.

[11] M. Jian and Y. Zhao, "A modified off-grid SBL channel estimation and transmission strategy for RIS-assisted wireless communication systems," in *Proc. Int. Wireless Commun. Mobile Comput. (IWCMC)*, Limassol, Cyprus, Jul. 2020, pp. 1848–1853.

[12] H. Liu, Y. Zhang, S. Gong, W. Shen, C. Xing, and J. An, "Optimal transmission strategy and time allocation for RIS-enhanced partially WPSNs," *IEEE Trans. Wireless Commun.*, vol. 21, no. 9, pp. 7207–7221, Sep. 2022.

[13] K. Liu, Z. Zhang, L. Dai, S. Xu, and F. Yang, "Active reconfigurable intelligent surface: Fully-connected or sub-connected?" *IEEE Commun. Lett.*, vol. 26, no. 1, pp. 167–171, Jan. 2022.

[14] Z. Zhang et al., "Active RIS vs. passive RIS: Which will prevail in 6G?" *IEEE Trans. Commun.*, vol. 71, no. 3, pp. 1707–1725, Mar. 2023.

[15] H. Sun, S. Zhang, J. Ma, and O. A. Dobre, "Path loss of RIS-aided spatial modulation with on/off pattern," *IEEE Commun. Lett.*, vol. 26, no. 4, pp. 937–941, Apr. 2022.

[16] S. Zhang, M. Li, M. Jian, Y. Zhao, and F. Gao, "AIRIS: Artificial intelligence enhanced signal processing in reconfigurable intelligent surface communications," *China Commun.*, vol. 18, no. 7, pp. 158–171, Jul. 2021.

[17] M. Cui, Z. Wu, Y. Lu, X. Wei, and L. Dai, "Near-field MIMO communications for 6G: Fundamentals, challenges, potentials, and future directions," *IEEE Commun. Mag.*, vol. 61, no. 1, pp. 40–46, Jan. 2023.

[18] X. Yu, D. Xu, and R. Schober, "MISO wireless communication systems via intelligent reflecting surfaces (invited paper)," in *Proc. IEEE/CIC Int. Conf. Commun. China (IEEE ICCC)*, Changchun, China, 2019, pp. 735–740.

[19] P. Wang, J. Fang, X. Yuan, Z. Chen, and H. Li, "Intelligent reflecting surface-assisted millimeter wave communications: Joint active and passive precoding design," *IEEE Trans. Veh. Technol.*, vol. 69, no. 12, pp. 14960–14973, Dec. 2020.

[20] H. Xie, J. Xu, and Y.-F. Liu, "Max-min fairness in IRS-aided multi-cell MISO systems with joint transmit and reflective beamforming," *IEEE Trans. Wireless Commun.*, vol. 20, no. 2, pp. 1379–1393, Feb. 2021.

[21] Q. Wu and R. Zhang, "Intelligent reflecting surface enhanced wireless network via joint active and passive Beamforming," *IEEE Trans. Wireless Commun.*, vol. 18, no. 11, pp. 5394–5409, Nov. 2019.

[22] C. Qi, K. Chen, O. Dobre, and G. Y. Li, "Hierarchical codebook-based multiuser beam training for millimeter wave massive MIMO," *IEEE Trans. Wireless Commun.*, vol. 19, no. 12, pp. 8142–8152, Dec. 2020.

[23] K. Chen, C. Qi, and G. Y. Li, "Two-step codeword design for millimeter wave massive MIMO systems with quantized phase shifters," *IEEE Trans. Signal Process.*, vol. 68, no. 1, pp. 170–180, Jan. 2020.

[24] K. Chen-Hu, G. Alexandropoulos, and A. Armada, "Differential data-aided beam training for RIS-empowered multi-antenna communications," *IEEE Access*, vol. 10, pp. 113200–113213, 2022.

[25] S. Jiang, A. Hindy, and A. Alkhateeb, "Camera aided reconfigurable intelligent surfaces: Computer vision based fast beam selection," Nov. 2022, *arXiv:2211.07563*.

[26] X. Wei, L. Dai, Y. Zhao, G. Yu, X. Duan, and X. Wang, "Codebook design and beam training for extremely large-scale RIS: Far-field or near-field?" *China Commun.*, vol. 19, no. 6, pp. 193–204, Jun. 2022.

[27] G. Alexandropoulos, V. Jamali, R. Schober, and V. Poor, "Near-field hierarchical beam management for RIS-enabled millimeter wave multi-antenna systems," Mar. 2022, *arXiv:2203.15557*.

[28] X. Shi, J. Wang, Z. Sun, and J. Song, "Chirp-based hierarchical beam training for extremely large-scale massive MIMO," Jan. 2023, *arXiv:2301.11570*.

[29] Y. Zhang, X. Wu, and C. You, "Fast near-field beam training for extremely large-scale array," *IEEE Wireless Commun. Lett.*, vol. 11, no. 12, pp. 2625–2629, Dec. 2022.

[30] K. Xu, F. Zheng, P. Cao, H. Xu, and X. Zhu, "Fast beam training for FDD multi-user massive MIMO systems with finite phase shifter resolution," *IEEE Trans. Veh. Technol.*, vol. 70, no. 1, pp. 459–473, Jan. 2021.

[31] S. Yang, Z. Zhang, Z. Hu, N. Song, and H. Liu, "Efficient multi-beam training for Terahertz wireless communications," Dec. 2021, *arXiv:2112.15346*.

[32] L. Dai et al., "Reconfigurable intelligent surface-based wireless communications: Antenna design, prototyping, and experimental results," *IEEE Access*, vol. 8, pp. 45913–45923, Mar. 2020.

[33] E. Basar, M. Di Renzo, J. De Rosny, M. Debbah, M. Alouini, and R. Zhang, "Wireless communications through reconfigurable intelligent surfaces," *IEEE Access*, vol. 7, pp. 116753–116773, Aug. 2019.

[34] J. Zhang, Y. Huang, J. Wang, X. You, and C. Masouros, "Intelligent interactive beam training for millimeter wave communications," *IEEE Trans. Wireless Commun.*, vol. 20, no. 3, pp. 2034–2048, Mar. 2021.

[35] O. El Ayach, S. Rajagopal, S. Abu-Surra, Z. Pi, and R. W. Heath, "Spatially sparse precoding in millimeter wave MIMO systems," *IEEE Trans. Wireless Commun.*, vol. 13, no. 3, pp. 1499–1513, Mar. 2014.

[36] Q. Nadeem, A. Kammoun, A. Chaaban, M. Debbah, and M. Alouini, "Intelligent reflecting surface assisted wireless communication: Modeling and channel estimation," Dec. 2019, *arXiv:1906.02360v2*.

[37] C. You, B. Zheng, and R. Zhang, "Fast beam training for IRS-assisted multiuser communications," *IEEE Wireless Commun. Lett.*, vol. 9, no. 11, pp. 1845–1849, Nov. 2020.

[38] X. Wei and L. Dai, "Channel estimation for extremely large-scale massive MIMO: Far-field, near-field, or hybrid-field?" *IEEE Commun. Lett.*, vol. 26, no. 1, pp. 177–181, Jan. 2022.
[39] C. Qi, P. Dong, W. Ma, H. Zhang, Z. Zhang, and G. Y. Li, "Acquisition of channel state information for mmWave massive MIMO: Traditional and machine learning-based approaches," *Sci. China Inf. Sci.*, vol. 64, no. 8, Aug. 2021, Art. no. 181301.
[40] Y. Sun, P. Babu, and D. P. Palomar, "Majorization-minimization algorithms in signal processing, communications, and machine learning," *IEEE Trans. Signal Process.*, vol. 65, no. 3, pp. 794–816, Feb. 2017.

Decai Shen received the B.E. degree (with highest Hons.) from Xidian University, Xi'an, China, in 2018. He is currently pursuing the Ph.D. degree in electronic engineering from Tsinghua University, Beijing, China. His research interests include reconfigurable intelligent surface with high spectral efficiency transmission. He has received the Honorary Mention in the 2019 IEEE ComSoc Student Competition.

Linglong Dai (Fellow, IEEE) received the B.S. degree from Zhejiang University, Hangzhou, China, in 2003, the M.S. degree (with Highest Hons.) from China Academy of Telecommunications Technology, Beijing, China, in 2006, and the Ph.D. degree (with Highest Hons.) from Tsinghua University, Beijing, in 2011.

From 2011 to 2013, he was a Postdoctoral Research Fellow with the Department of Electronic Engineering, Tsinghua University, where he was an Assistant Professor from 2013 to 2016, an Associate Professor from 2016 to 2022, and has been a Professor since 2022. He has authored or coauthored over 80 IEEE journal articles and over 50 IEEE conference papers. He also holds 19 granted patents. He has coauthored the book *MmWave Massive MIMO: A Paradigm for 5G* (Academic Press, 2016). Particularly, he is dedicated to reproducible research and has made a large amount of simulation code publicly available. His current research interests include massive MIMO, reconfigurable intelligent surface, millimeter-wave and Terahertz communications, machine learning for wireless communications, and electromagnetic information theory.

ÂăDr. Dai has received five IEEE Best Paper Awards at the IEEE ICC 2013, the IEEE ICC 2014, the IEEE ICC 2017, the IEEE VTC 2017-Fall, and the IEEE ICC 2018. He has also received the Tsinghua University Outstanding Ph.D. Graduate Award in 2011, the Beijing Excellent Doctoral Dissertation Award in 2012, the China National Excellent Doctoral Dissertation Nomination Award in 2013, the URSI Young Scientist Award in 2014, the IEEE TRANSACTIONS ON BROADCASTING Best Paper Award in 2015, the *Electronics Letters* Best Paper Award in 2016, the National Natural Science Foundation of China for Outstanding Young Scholars in 2017, the IEEE ComSoc Asia–Pacific Outstanding Young Researcher Award in 2017, the IEEE ComSoc Asia–Pacific Outstanding Paper Award in 2018, the China Communications Best Paper Award in 2019, the IEEE ACCESS Best Multimedia Award in 2020, the IEEE Communications Society Leonard G. Abraham Prize in 2020, and the IEEE ComSoc Stephen O. Rice Prize in 2022, and the IEEE ICC Outstanding Demo Award in 2022. He was listed as a Highly Cited Researcher by Clarivate Analytics from 2020 to 2022. He is currently serving as an Area Editor for the *IEEE Communications Letters*, and an Editor for the IEEE TRANSACTIONS ON WIRELESS COMMUNICATIONS. He has also served as an Editor for the IEEE TRANSACTIONS ON COMMUNICATIONS from 2017 to 2021, the IEEE TRANSACTIONS ON VEHICULAR TECHNOLOGY from 2016 to 2020, and the IEEE COMMUNICATIONS LETTERS from 2016 to 2020. He has also served as a Guest Editor for the IEEE JOURNAL ON SELECTED AREAS IN COMMUNICATIONS, IEEE JOURNAL OF SELECTED TOPICS IN SIGNAL PROCESSING, and IEEE WIRELESS COMMUNICATIONS.

Xin Su received the B.S., M.S., and Ph.D. degrees from Xidian University, Xi'an, China in 2000, 2003, and 2006, respectively. From 2006 to 2007, he was with the System and Standard Department, Datang Mobile, CATT, Beijing, China. In 2007, he joined the System Lab, Telecommunication System Division, Samsung Electronics, Suwon, South Korea. Since 2011, he has been with the Datang Wireless Mobile Innovation Center, CATT. He is currently a Senior Engineer with CICT Mobile Communications Technology Company Ltd., Beijing. His research interests are multiantenna system and its standardization in radio access networks.

Shiqiang Suo received the B.S. degree in automation from Tsinghua University, China, in 1999, and the M.A. degree in communication and information system from the China Academy of Telecommunication Technology, China, in 2002. He has long-term engaged in wireless mobile communication system (including 3G, 4G, 5G, and 6G) new technology research, verification and standardization (including 3GPP, ITU-R, and O-RAN alliance), and has obtained more than 400 authorized invention patents. He is currently a Vice General Manager of Innovation Center with CICT Mobile Communication Technology Company Ltd., and responsible for the research of 6G and future new technologies, mainly focusing on massive MIMO, AI, integrated sensing and communication, and wireless network architecture.